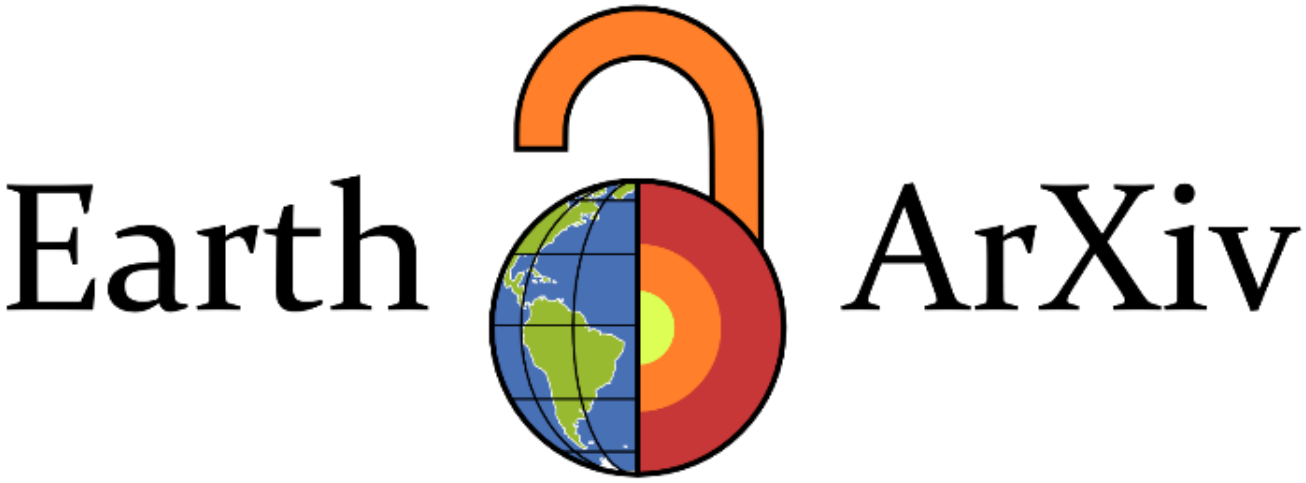

Preprint Status Statement:

This manuscript is a non-peer-reviewed preprint submitted to EarthArXiv.

End-to-End Differentiable Auto-Calibration of a Distributed Glacio-Hydrological Model Using Physically Consistent Routing

Dinesh Joshi[1], Kundan Lal Shrestha[3], and Rijan Bhakta Kayastha[2]
[1]Independent Researcher
[2]Department of Environmental Science and Engineering, School of Science, Kathmandu University, Dhulikhel, 45210, Nepal
[3]Department of Chemical Science and Engineering, School of Engineering, Kathmandu University, Dhulikhel, 45210, Nepal

Correspondence: Dinesh Joshi (joshidinesh0227@gmail.com)

Abstract.

Distributed glacio-hydrological models are essential for simulating runoff processes in glacier-fed Himalayan basins, yet their application is often constrained by extensive data requirements, high computational costs, and reliance on manual, trial-and-error calibration. Recent auto-calibration approaches using stochastic optimization or machine learning have shown promise, but they frequently suffer from limited physical interpretability, high computational demand, or the absence of physically consistent routing formulations, restricting their applicability to spatially distributed models. In this study, we present an end-to-end differentiable, gradient-based auto-calibration framework for the PCRaster-based PyGDM glacio-hydrological model. The framework integrates a physically consistent, mass-conserving routing scheme based on an eight-direction flow network, implemented in TensorFlow and optimized using Accelerated Linear Algebra (XLA). This formulation enables gradient propagation through all hydrological processes, including surface runoff generation, subsurface flow, and river routing, allowing simultaneous calibration of spatially and temporally varying parameters directly from discharge observations. Spatially distributed subsurface parameters and monthly varying surface and cryospheric parameters are optimized using automatic differentiation and constrained within physically meaningful ranges through sigmoid-based reparameterization. To address the lack of spatial discharge observations, a flow-accumulation-based pseudo-observed discharge field is constructed to support spatially distributed calibration. The framework is evaluated in the glacier-fed Bheri Basin, Nepal, and benchmarked against a manually calibrated PyGDM simulation. Results demonstrate that the proposed approach outperforms manual calibration, achieving higher predictive skill during both calibration (NSE = 0.85; VD = −6.56) and validation (NSE = 0.86; VD = −0.06) periods, while requiring substantially reduced human intervention. The learned parameters exhibit coherent spatial, elevation-dependent, land-use-specific, and seasonal patterns that remain physically interpretable and consistent with hydrological understanding of Himalayan catchments. The study demonstrates that fully differentiable, physically constrained routing is critical for robust end-to-end calibration of distributed hydrological models. The proposed framework offers a scalable, computationally efficient, and physically interpretable solution for auto-calibration in data-limited, glacier-fed basins, with broad applicability to high-resolution hydrological modeling and climate impact assessments.

Introduction

Different glacio-hydrological modelling approaches have been developed in the Himalayan region to support large-scale studies, but the extensive data requirements and high computational costs limit their wider application. Various studies using empirical and process-based approaches, such as energy-balance glacier models (Shrestha et al., 2015), distributed hydrological models (Garee et al., 2017; Shukla et al., 2021; Wulf et al., 2016), WASMOD with WRF-derived precipitation (Li et al., 2019), VIC-glacier and VIC-GM2 (Wang et al., 2021; Chandel and Ghosh, 2021), and ANN models (Buch et al., 1993) illustrate these efforts.

To advance the above objective, the distributed framework of the PCRaster-based PyGDM implementation (Shrestha et al., 2024), built upon the parsimonious structure of the Glacio-Hydrological Degree-Day Model (GDM; Kayastha et al., 2020), provides a balanced modelling strategy suita-

ble for data-limited, glacier-fed Himalayan basins. The distributed and flexible nature of PyGDM also allows the integration of spatially heterogeneous and monthly-varying auto-calibrated parameters, which is feasible for the study.

A recent study on auto-calibration (Feng et al., 2025) demonstrates improvements in both accuracy and computational efficiency compared to the traditional trial-and-error method. Meanwhile, advances in computational resources have facilitated the mainstream adoption of auto-calibration approaches (Shahed Behrouz et al., 2020). The uncertainty and reliance on user expertise inherent in the trial-and-error method (Ma et al., 2022) further underscore the importance of developing auto-calibration strategies.

The three broad auto-calibration strategies in hydrological modeling are: (i) near-random sampling, (ii) nature-inspired optimization, and (iii) artificial neural networks (ANN). While these methods have been successfully applied for hydrological parameter calibration, the exclusive use of any single approach has limitations, including high computational cost, stochastic convergence, large data requirements, and challenges with spatially heterogeneous parameters.

For example, near-random sampling methods, such as Monte Carlo Simulation (MCS) and Latin Hypercube Sampling (LHS), identify optimal parameters by exploring different combinations across the entire range of possible values (Schneider & Hogue, 2022; Zhang et al., 2022b; Sun et al., 2020; Barco et al., 2008). This approach is computationally expensive and becomes impractical for spatially heterogeneous parameters because the number of parameter combinations increases astronomically.

Nature-inspired optimization methods, on the other hand, mimic processes observed in nature to search for optimal model parameters. These include algorithms such as bee or ant colony methods, evolutionary algorithms (Sun et al., 2021; Leta et al., 2017; Kang & Lee, 2014), genetic algorithms (Zhong et al., 2022), and particle swarm optimization (Wang et al., 2019; Jafari et al., 2018; Xue et al., 2020). Unlike near-random sampling, these methods iteratively update parameters toward convergence using mechanisms inspired by natural processes. Despite their advantages, they are computationally expensive and may suffer from poor stochastic convergence.

Finally, artificial neural networks (ANNs) use gradient-based optimization to adjust model parameters and learn the relationships between input and output variables. Li et al. (2024) applied an LSTM-based ANN, while Feng et al. (2024) employed a back-propagation (BP) ANN, with both studies demonstrating successful auto-calibration of hydrological models. Beyond calibration, ANNs can also facilitate parameter screening; for instance, Wu et al. (2021) used a binary-classification ANN to efficiently identify sensitive SWMM parameters, achieving over 96% accuracy in parameter prediction. Despite these advantages, ANN-based approaches generally require large training datasets to ensure reliable calibration performance (Cai et al., 2021) and are often criticized for their limited physical interpretability.

To overcome the limitations of purely gradient-based learning, coupling hydrological processes with gradient-based models has gained increasing attention. Broadly, two coupling strategies exist**:** one-way coupling and two-way coupling**.** In a one-way coupled approach, there is no feedback from the gradient-based component to the physical model. For example, Joshi et al. (2024) trained recurrent neural networks on the residual errors of a process-based glacier hydrological model, while Xu et al. (2022) used simulated snowmelt from a distributed physical snow model to train a ConvLSTM for streamflow prediction. In both cases, the routing process remains effectively a black box because the gradient-based component does not influence the physical simulation.

Two-way coupling can alleviate this issue by integrating physical knowledge directly into the gradient-based component, enabling the joint optimization of physical parameters and yielding more physically interpretable results. However, the main challenge lies in constructing a physically consistent, differentiable routing process**.** Several studies have made progress in embedding physical knowledge into machine learning to combine the strengths of both approaches (M. Chen et al., 2023; Kraft et al., 2022; Höge et al., 2022), as initially advocated by Reichstein et al. (2019). For instance, Jiang et al. (2020) and Feng et al. (2022) embedded the conceptual models EXP-HYDRO and Hydrologiska Byråns Vattenbalansavdelning (HBV), respectively, within deep-learning architectures to improve runoff simulation. However, due to the absence of a physically consistent gradient-based routing formulation, these hybrid models remain spatially lumped. They therefore

cannot represent internal watershed heterogeneity or explicitly simulate river routing, and instead rely on lumped parameters to predict discharge only at the basin outlet. Bindas et al. (2024) and Sun et al. (2022) explored deep-learning-based approaches for distributed routing, but important limitations remain. Bindas et al. combined LSTMs for sub-basin runoff generation with a physics-based neural network for river routing; however, the two components were trained separately, preventing true end-to-end optimization. Sun et al. applied Graph Neural Networks (GNNs) to represent river topology and support flow routing, yet GNNs still face challenges in generalizing across basins with differing hydroclimatic characteristics and do not inherently conserve water unless physical constraints are explicitly enforced. Collectively, these studies show promising progress but also highlight that a unified, physically consistent, end-to-end differentiable hydrological modeling framework is still lacking.

To address the aforementioned limitations, Wang et al. (2024) proposed HydroPy-DL, an end-to-end differentiable framework; however, the spatially distributed parameters are estimated through a learned attribute-to-parameter mapping rather than being directly auto-calibrated from discharge, which may limit true physical parameter identification and the sensitivity of parameters to model outputs.

The present study aims to auto-calibrate spatially and temporally varying parameters from PyGDM using an end-to-end differentiable framework. We employ an XLA (Accelerated Linear Algebra)-optimized differentiable routing function, which leverages eight-directional topological ordering to compute river routing efficiently and physically consistently, enabling the joint auto-calibration of multiple parameters directly from discharge through gradient propagation across the routing process.

Methodology

The model architecture is built on TensorFlow to leverage the automatic differentiation feature to calculate the exact analytical gradient of parameters with respect to the loss function with machine-level precision. Automatic differentiation breaks the function into elementary operations, applies the chain rule programmatically, and accumulates derivatives.

The physical backbone of the model is based on the PyGDM framework and is implemented in TensorFlow (Fig. 1). All hydrological processes are computed in a distributed manner across the spatial grid. Precipitation is classified as either rain or snow based on a threshold temperature (Eq. 1), where T represents the grid-wise air temperature and T_t is the threshold temperature, both expressed in degrees Celsius. Snowmelt and ice melt, M (mm d^{-1}), are calculated using degree-day factors for snow, bare ice, and debris-covered ice (Eq. 2), where T is air temperature (°C), Ks is the degree-day factor for snow (mm $°C^{-1}$ d^{-1}), Kb is the degree-day factor for bare ice (mm $°C^{-1}$ d^{-1}), and Kd is the degree-day factor for debris-covered ice (mm $°C^{-1}$ d^{-1}).

$$precipitation = \begin{cases} rain, if \;\; T \geq T_t \\ snow, if \;\; T < T_t, \end{cases} \quad (1)$$

$$M = \begin{cases} K_d \text{ or } K_s \text{ or } K_b * \mathrm{T}, & if, T > 0 \\ 0, & if, T \leq 0, \end{cases} \quad (2)$$

Potential evapotranspiration (PET) is estimated using the Hargreaves method based on temperature data. The Hargreaves method computes PET using Eq. (3), where PET is potential evapotranspiration (mm d^{-1}), T_{mean} is the average daily temperature (°C), T_{max} is the maximum daily temperature (°C), T_{min} is the minimum daily temperature (°C), and R_a is extraterrestrial radiation (MJ m^2 d^{-1}), which is calculated as a function of location, date, and time using established formulations. Interception is estimated using a simple interception model with predefined monthly threshold values (I, mm d^{-1}).

$$PET = 0.0023\,(T_{mean} + 17.8)\,R_a\;0.0408\,\sqrt{T_{max} - T_{min,}} \quad (3)$$

Surface runoff generated from rainfall, snowmelt, and ice melt is computed using land-use-specific runoff coefficients (Rc), while the remaining water contributes to baseflow. Baseflow is simulated using the two-reservoir modeling approach adopted in SWAT (Luo et al., 2012). The key processes considered in baseflow simulation include percolation of surface water (Wseep), the delay time for percolation in the shallow aquifer due to overlying geological formations (δsh), the recession constant of the shallow aquifer (αsh), the seepage constant governing percolation to the deep aquifer (βdp), the delay time for deep aquifer percolation (δdp), and the recession constant of the deep aquifer (αdp). The rainfall, snowmelt, and ice-melt-

driven surface flow components are temporally routed using a routing coefficient (kx), which controls the relative contribution of current and previous timestep flows. Total discharge is obtained as the sum of baseflow and all surface flow components.

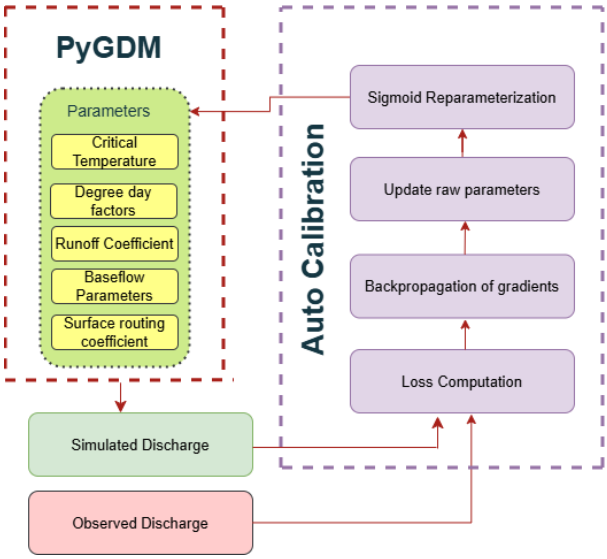

Figure 1. Schematic workflow of the study showing the sequence of steps from meteorological and spatial data inputs, through PyGDM hydrological model implementation and end-to-end differentiable auto-calibration.

Differentiable Routing Framework

We used a differentiable flow routing scheme implemented in TensorFlow and conceptually based on the PCRaster local drain direction (LDD) framework. The scheme follows an eight-direction (D8) flow network and performs flux accumulation using a topological ordering of grid cells, ensuring mass-conserving upstream-to-downstream routing. All routing computations are fully differentiable, allowing gradients to propagate through the flow network and enabling end-to-end, gradient-based model calibration. The routing kernel is compiled using TensorFlow's XLA compiler to enhance computational efficiency and scalability.

Model Optimization and Training

To calibrate the spatially distributed process-based model, we define mean squared error based loss functions that measure the mismatch between simulated and spatially inferred observed discharge. Because direct spatial observations are unavailable, we construct a spatial pseudo-observed discharge field based on outlet observations and model flow accumulation. Eq. (4) represents spatial pseudo-observed discharge where $W(x,y)$ is a normalized flow-accumulation-based weighting factor that increases downstream, and ε is a small constant added for numerical stability. Q_{obs} and Q_{sim}^{out} are observed and simulated discharge at the outlet respectively.

$$Q_{pseudo}(x,y) = Q_{sim}(x,y)\left[1 + W(x,y)\frac{Q_{obs} - Q_{sim}^{out}}{Q_{sim}^{out} + \varepsilon}\right] \quad (4)$$

$$L = \frac{1}{N}\sum(Q_{sim} - Q_{pseudo})^2 \quad (5)$$

Eq. (5) represents loss responsible for calibrating the parameters. Where, Q_{sim} is spatially distributed simulated discharge and Q_{pseudo} is spatially distributed pseudo observed discharge.

Table 1. Physical ranges and units of the model parameters used in the PyGDM setup.

Parameter		Physical Range	Unit
K_b		6 – 9	mm °C d^{-1}
K_d		1.5 – 3	mm °C d^{-1}
K_s		2 – 5.5	mm °C d^{-1}
δ_{sh}		10 – 30	days
δ_{dp}		10 – 300	days
α_{sh}		0 – 1	/
α_{dp}		0 – 1	/
β_{dp}		0 – 1	/
	Forest	0.2 – 0.7	/
	Agriculture	0.4 – 0.8	/
	Grassland	0.5 – 0.8	/
	Barren land	0.3 – 0.7	/
	Water bodies	0.9 – 1	/
R_c	Built-up area	0.9 – 1	/
	Debris-covered glacier	0.95 – 1	/
	Clean/bare glacier	0.95 – 1	/
K_x		0-1	/
	Forest	1.2-5.7	mm d^{-1}
	Agriculture	0.6-2.3	mm d^{-1}
	Grassland	0.3-1.2	mm d^{-1}
I	Debris-covered glacier	0-0.5	mm d^{-1}
	Clean/bare glacier	0-0.5	mm d^{-1}

Gradients of the monthly loss with respect to all trainable parameters are computed at each daily timestep using TensorFlow's GradientTape, which applies reverse-mode automatic differentiation. Gradients are accumulated over all days within the month, averaged, and used to update parameters for that month. Model parameters are optimized

using the Adam optimizer and a uniform learning rate of 0.01 was applied to all trainable parameters. To maintain physical realism, each parameter is initialized as a raw variable and transformed using a sigmoid-based scaling function within predefined physical ranges (Table 1).

Parameters that exhibit strong spatial dependence, such as subsurface delay times (δsh, δdp), recession constants (αsh, αdp) and baseflow partition coefficient (βdp) are trained as grid-level tensors. Parameters with seasonal variation (e.g., Kb, Kd, Rc) are trained as monthly variables, with land-use-specific parameterizations where the sigmoid scaling is applied separately for each land-cover type. The snow-melt factor (Ks) is trained only over the snow-covered domain with monthly variation, and the routing coefficient (kx) is trained with monthly variation.

The model operates at daily timesteps, with monthly accumulation of gradients and parameter updates. Training continues until convergence of the loss function toward a global minimum. Overall, the workflow is implemented in TensorFlow, enabling end-to-end differentiable hydrological simulation from meteorological forcing inputs to discharge prediction within a single computational graph.

Input data

The PyGDM hydrological model utilizes satellite-derived topographic and land-surface datasets. Land use and land cover (LULC) (Fig. 2) information was obtained from the ESRI global land cover product derived from Sentinel-2 imagery (10 m resolution) (Karra et al., 2021; last accessed November 2025). The original ten LULC classes were reclassified into eight hydrologically relevant categories; forest, grassland, agriculture, barren land, water bodies, built-up areas, debris-covered glaciers, and clean/bare glaciers based on similar surface characteristics and runoff responses. Topographic data were represented using the SRTM 1-arcsecond global DEM (≈30 m resolution) acquired from the USGS EarthExplorer (last accessed November 2025). Glacier extent was incorporated using outlines from the Randolph Glacier Inventory (RGI v6.0) (Arendt et al., 2017), which also supported land cover reclassification.

Meteorological forcing data, including daily precipitation and maximum and minimum air temperature, were otained from the Department of Hydrology and Meteorology (DHM), Nepal, from eight stations located at different elevations within the Bheri basin. Both DEM and LULC were resampled to 180 m grid to prepare meteorological data and to execute hydrological simulation. Precipitation was spatially interpolated using the inverse distance weighting (IDW) method, while temperature was distributed using an elevation-based lapse rate. Daily discharge observations from the Samaijighat hydrological station (≈500 m a.s.l.) were used for model calibration and validation (Table 2).

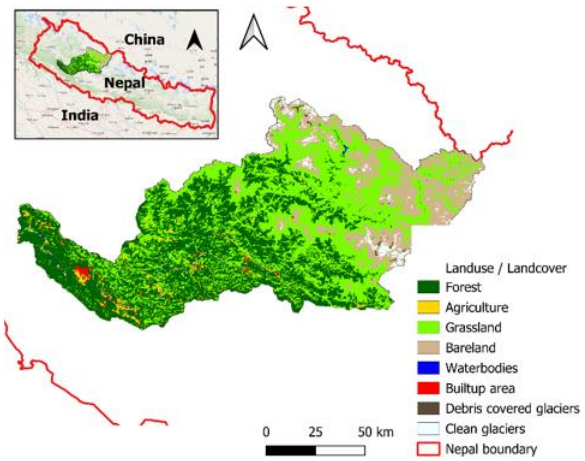

Figure 2. Land use and land cover (LULC) of Bheri River basin.

Results and Discussion

Model Calibration Performance

To benchmark the proposed end-to-end auto-calibration framework, we reproduced the manually calibrated PyGDM simulation for the Bheri Basin reported by Rakesh et al. (2024). To ensure a controlled and equitable comparison, we adopted the same calibration (2004–2010) and validation (2011–2017) periods (Fig. 3), identical spatial resolution of input datasets, and the same evaluation metrics: Nash–Sutcliffe Efficiency (NSE) and Volume Difference (VD).

During the calibration period, the proposed gradient-based framework achieved an NSE of 0.85 and a VD of -6.56, improving upon the manually calibrated results of NSE = 0.82 and VD = 4.5 reported by Rakesh et al. (2024). More notably, during the independent validation period, our model maintained strong predictive skill with an NSE of 0.86 and a VD of −0.06,

whereas the reference study showed a marked degradation in performance (NSE = 0.71; VD = −5.3). In contrast to the manual calibration process, which required extensive trial-and-error and expert intervention over prolonged periods, the gradient-based framework fully automated parameter optimization, achieving improved performance with minimal human effort and substantially reduced time. The consistent improvement across both calibration and validation phases indicates enhanced generalization and reduced parameter overfitting relative to manual calibration. These results provide strong evidence that gradient-based, end-to-end auto-calibration is not only computationally viable but also methodologically robust for distributed, physically based glacio-hydrological models provided that the routing scheme is fully differentiable and strictly mass-conversing.

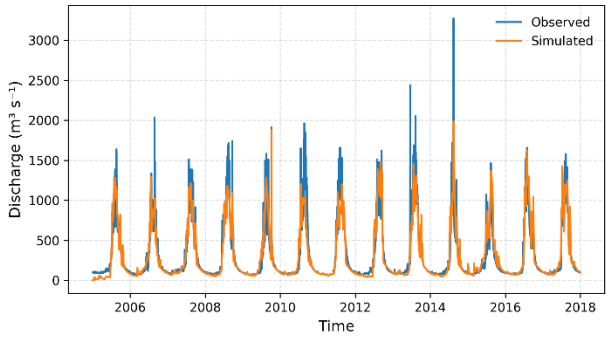

Figure 3. Comparison of observed and simulated daily discharge ($m^3\ s^{-1}$) for the period 2005–2007.

Surface-Flow and Baseflow Parameter Learning

The calibrated snow and ice melt parameters exhibit clear seasonal variability while remaining within physically plausible ranges (Table 3), reflecting temperature-controlled cryospheric processes in the basin. The snowmelt degree-day factor (Ks) is lowest during winter, increases through the pre-monsoon and monsoon periods, and peaks in August, indicating enhanced snowmelt contributions to streamflow during warmer months, before declining again in the post-monsoon with decreasing temperatures, with mid-monsoon moderation reflecting persistent snow cover and energy limitations. The ice melt coefficient (Kb) follows a similar seasonal pattern, with lower values in spring and early summer and higher values in late summer and early autumn, corresponding to maximum glacier melt under peak seasonal temperatures. In contrast, the debris-covered ice melt factor (Kd) remains lower during pre-monsoon due to insulating debris and residual snow cover, but increases during late summer and post-monsoon as elevated temperatures and reduced snow cover enhance energy transfer to debris-covered ice. Collectively, these seasonal responses are consistent with the climatology of Himalayan catchments and reflect realistic cryospheric melt dynamics. The surface routing coefficient (Kx) exhibits a clear seasonal pattern and remains within our predefined physical range (Table 3). It peaks in May when current-timestep runoff is low, so most flow is carried over from previous timesteps, producing a delayed and smoothed hydrograph. During the monsoon, moderate values allow the hydrograph to respond promptly to high runoff while retaining some temporal smoothing. Post-monsoon and early winter show the lowest values, reflecting minimal flow persistence and rapid event-driven runoff through a fully established surface drainage network. Winter months maintain intermediate values, consistent with gradual snowmelt inputs and moderate temporal persistence of surface flow. The trained surface runoff and interception parameters exhibit clear monthly seasonal patterns and remain within predefined physically plausible ranges (Table 4 and 5). Across all land-use classes, runoff coefficients are lower during dry months and higher during the monsoon, while interception capacity shows the opposite behavior, with higher values in dry periods and reduced capacity during the monsoon. Bareland, water bodies, and built-up areas are assigned zero interception capacity in accordance with their predefined physical ranges.

Table 2. List of the climatological and hydrological stations in the study area.

Basin	Station (m a.s.l.), type	Hydrological station	Year
Bheri River	Dunai (2098), precipitation; Mainagau (1913), precipitation; Rukumkot (1568), precipitation; Musikot (1412), climatology; Jagarkot (1240), climatology; Chaurjhar (863), climatology; Surkhet (720), synoptic	Samaijighat	2004–2017

Table 3. Monthly calibrated degree-day factors for snow (Ks), bare ice (Kb), and debris-covered ice (Kd) (mm $°C^{-1}$ d^{-1}), and the surface routing coefficient (Kx).

Month	Ks	Kb	Kd	Kx
Jan	2	7.5	2.2	0.82
Feb	2	6.6	1.8	0.91
Mar	2	6	1.5	0.84
Apr	2	6	1.5	0.88
May	3.9	6	1.5	0.97
Jun	2	6	1.5	0.95
Jul	2	6	1.5	0.81
Aug	5.5	9	3	0.91
Sep	2.1	9	3	0.83
Oct	2.9	9	3	0.56
Nov	2	6	1.5	0.91
Dec	2	7.5	2.2	0.83

These contrasting seasonal responses are consistent with expected canopy storage dynamics and reflect realistic hydrological behavior. The seasonal variability in interception represents an effective storage response under prevailing hydro-meteorological conditions rather than a change in static canopy structure.

The optimized baseflow parameters remain within the predefined physically plausible ranges (Fig 4). Table 6 shows clear and physically consistent elevation-dependent patterns across the basin of the learned baseflow parameters. The deep percolation partitioning parameter (β_dp) increases systematically from low-elevation foothills (0.29 ± 0.35) to high mountain regions (0.98 ± 0.08), indicating an increasing contribution of deep subsurface flow with elevation, likely associated with steeper terrain, thinner soils, and enhanced vertical drainage pathways. Correspondingly, the deep aquifer recession constant (α_dp) decreases with elevation, suggesting progressively longer groundwater residence times and delayed baseflow response in high-elevation zones. The deep percolation delay (δ_dp) shows a monotonic increase from lowlands to high mountains, consistent with increasing subsurface flow path lengths and storage depth at higher elevations.

Shallow aquifer parameters display comparatively weaker elevation sensitivity. The shallow recession constant (α_sh) remains low across most elevation bands, reflecting generally slow shallow groundwater drainage, while the shallow percolation delay (δ_sh) is relatively stable (~25 days) in mid-elevation zones and slightly reduced at both low and high elevations, indicating limited topographic control on shallow storage timescales.

In contrast, all baseflow parameters in the highest elevation band (6300–7424 m) converge toward the midpoint of their predefined physical ranges with negligible spatial variability. This limited variability reflects the dominance of snow and ice melt processes in these regions, where degree-day melt parameters primarily control runoff generation, thereby reducing the sensitivity of outlet discharge to subsurface flow parameters and limiting their identifiability through discharge-based calibration.

Within each elevation band, the mean value of both shallow and deep subsurface parameters exhibit systematic variation across land use and land cover (LULC) classes. The parameter α_sh consistently attains its lowest values in vegetated classes (forest, agriculture, and grassland), whereas bareland, waterbodies, and built-up areas exhibit markedly higher values. In high-elevation zones, glacier-related land uses (debris-covered and clean glaciers) show substantially elevated α_sh, approaching upper-bound values, suggesting a rapid shallow flow response in cryospheric terrains.

Across elevation bands, δ_sh is consistently highest in bareland, followed by forest, agriculture, and grassland, while waterbodies and built-up areas show systematically lower values. At higher elevations, glacier-covered classes (debris-covered and clean glaciers) exhibit the lowest and nearly constant δ_sh values (~20–21), and overall land-use contrasts diminish, indicating reduced sensitivity of δ_sh to surface characteristics in cryospheric zones.

The parameter δ_dp shows lowest values in vegetated classes (forest and agriculture), with progressively higher values in grassland and bareland. Waterbodies and built-up areas consistently exhibit high δ_dp. At higher elevations, glacier-influenced classes (debris-covered and clean glaciers) display among the highest δ_dp values, comparable to or exceeding those of non-vegetated surfaces.

The parameter α_dp attains its highest values in forest and agricultural areas, with intermediate values in grassland and bareland, while waterbodies and built-up areas consist-

ently show low values. At higher elevations, glacier-influenced classes (debris-covered and clean glaciers) display minimal α_dp.

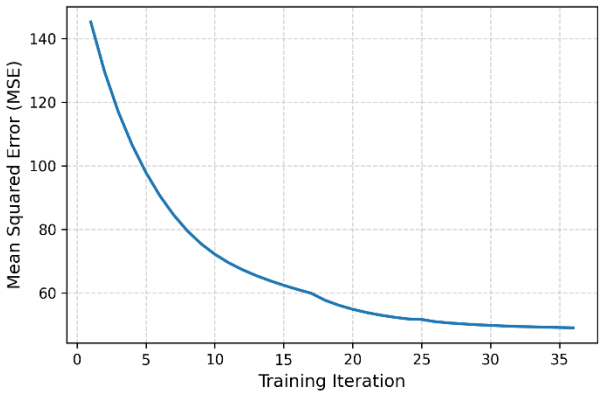

Figure 5. Evolution of the mean squared error (MSE) during parameter training, indicating stable convergence of the optimization process.

The parameter β_dp exhibits lowest values in forest and agricultural areas at lower elevations, with intermediate to high values in grassland and bareland. Waterbodies and built-up areas consistently exhibit high β_dp, and at higher elevations, glacier-influenced classes (debris-covered and clean glaciers) display the highest values, often exceeding those of non-vegetated surfaces. Overall, comparison across parameters indicates that β_dp and α_sh are the most sensitive to LULC, followed by δ_dp and δ_sh, while α_dp shows comparatively weaker but consistent dependence. The complete set of parameter values supporting these findings is provided in the supplementary material (Table S1). The gradient-based optimization exhibited stable convergence behavior across training epochs, characterized by a smooth and monotonic reduction in the loss function with no evidence of oscillatory or divergent updates (Fig. 5). Parameter trajectories remained within predefined physical bounds throughout training, indicating that the reparameterization strategy effectively constrained the optimization while preserving gradient flow. Convergence was achieved without manual tuning or restart, highlighting the robustness of the optimization procedure.

Despite its end-to-end differentiable formulation, the proposed framework remained computationally tractable for basin-scale application, converging within 36 epochs (≈ 12 hours of wall-clock time on a personal laptop using a 4 GB RAM CPU and using a learning rate of 0.01).

Table 4. Monthly surface runoff parameter by land-use classes. Values are constrained within the physically defined, class-specific ranges used during model training.

Land-use class	Jan	Feb	Mar	Apr	May	Jun	Jul	Aug	Sep	Oct	Nov	Dec
Forest	0.2	0.2	0.2	0.24	0.2	0.7	0.7	0.7	0.7	0.7	0.2	0.2
Agriculture	0.4	0.8	0.4	0.4	0.4	0.8	0.8	0.8	0.8	0.8	0.4	0.4
Grassland	0.5	0.5	0.5	0.5	0.5	0.7	0.5	0.8	0.8	0.76	0.5	0.5
Bareland	0.3	0.7	0.3	0.32	0.3	0.3	0.31	0.7	0.7	0.7	0.3	0.3
Waterbodies	0.9	0.99	0.9	0.9	0.9	0.99	0.99	0.99	0.99	0.99	0.90	0.90
Builtup areas	0.9	0.99	0.90	0.90	0.90	0.99	0.99	0.99	0.99	0.99	0.90	0.90
Debris-covered glaciers	0.98	0.96	0.95	0.95	0.95	0.95	0.96	0.99	0.99	0.99	0.95	0.98
Clean glaciers	0.98	0.96	0.95	0.95	0.95	0.95	0.97	0.99	0.99	0.99	0.95	0.98

The model formulation is inherently GPU-compatible, and substantially reduced training times are expected under GPU acceleration, while enabling fully automated spatial parameter learning without manual intervention. A higher learning rate of 0.1 substantially reduced training time and the number of epochs required for convergence, with only minor non-monotonic variations near the final stages.

Despite the high dimensionality of the parameter space, the learned parameters exhibit structured spatial and seasonal patterns rather than arbitrary compensation, suggesting partial mitigation of equifinality through joint optimization of all processes. Nevertheless, reduced parameter variability and convergence toward mid-range values in the highest elevation band indicate limited identifiability of subsurface parameters in cryosphere-dominated regions,

Table 5. Monthly trained interception parameters (mm/day) for different land-use classes. Values are constrained within the physically defined, class-specific ranges used during model training.

Land-use class	Jan	Feb	Mar	Apr	May	Jun	Jul	Aug	Sep	Oct	Nov	Dec
Forest	5.69	5.69	5.68	5.66	5.69	4.86	5.65	1.2	1.2	1.21	5.69	5.69
Agriculture	2.29	0.6	2.29	2.29	2.29	0.64	2.24	0.6	0.6	0.6	2.29	2.29
Grassland	1.19	1.19	1.19	1.19	1.19	1.19	1.19	0.3	0.3	0.3	1.19	1.19
Bareland	0.0	0.0	0.0	0.0	0.0	0.0	0.0	0.0	0.0	0.0	0.0	0.0
Waterbodies	0.0	0.0	0.0	0.0	0.0	0.0	0.0	0.0	0.0	0.0	0.0	0.0
Builtup areas	0.0	0.0	0.0	0.0	0.0	0.0	0.0	0.0	0.0	0.0	0.0	0.0
Debris-covered glaciers	0.25	0.42	0.48	0.49	0.50	0.50	0.50	0.0	0.0	0.0	0.36	0.25
Clean glaciers	0.25	0.37	0.41	0.49	0.50	0.50	0.49	0.0	0.0	0.0	0.31	0.25

where discharge sensitivity is governed primarily by melt processes. Together, these results demonstrate that physically constrained, gradient-based calibration can simultaneously improve predictive skill and yield interpretable parameter fields in complex glacio-hydrological systems.

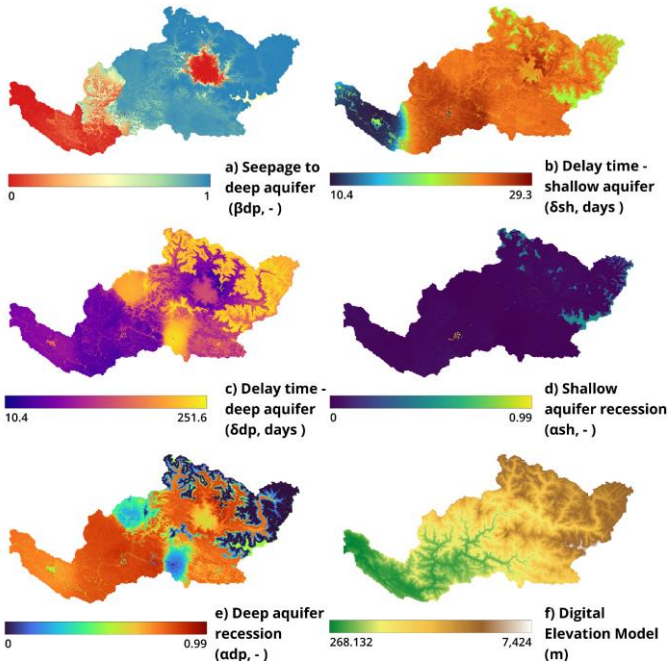

Figure 4. Spatial distribution of calibrated baseflow parameters (β_dp, α_sh, δ_sh, α_dp, δ_dp) and the digital elevation model (DEM) across the study basin.

Effectiveness of Differentiable Routing

The effectiveness of the proposed gradient-based calibration framework critically depends on the use of a fully differentiable and strictly mass-conserving routing scheme. By enabling gradient propagation through upstream–downstream flow accumulation over the D8 flow network, the routing formulation allows hydrological parameters across the basin to be optimized directly with respect to outlet discharge. The smooth and monotonic reduction of the loss function during training, together with the absence of oscillatory or divergent updates, indicates that routing-related gradients remained numerically stable throughout optimization.

The mass-conserving nature of the routing scheme ensures that gradient propagation does not introduce artificial gains or losses of water, preserving physical consistency during parameter learning. This is reflected in the physically coherent spatial and seasonal patterns of the optimized parameters and in the improved validation performance relative to manual calibration. In contrast to conventional hydrological workflows where routing is fixed and non-differentiable, the proposed formulation enables runoff generation, subsurface flow, and streamflow routing to be optimized jointly in a unified end-to-end framework. These results confirm that differentiable routing is not merely computationally feasible, but essential for achieving robust, interpretable, and generalizable calibration in distributed glacio-hydrological models.

Future Extensions and Limitations

While the current framework demonstrates robust performance using outlet-based calibration, its flexibility allows

Table 6. Mean and standard deviation of calibrated baseflow parameters across elevation bands in the Bheri Basin.

Elevation Band (m)	Description / Zone	β_dp (Mean ± SD)	α_sh (Mean ± SD)	δ_sh (Mean ± SD)	α_dp (Mean ± SD)	δ_dp (Mean ± SD)
268 – 1500	Lowlands / Foothills	0.285 ± 0.346	0.029 ± 0.059	19.798 ± 6.875	0.763 ± 0.104	77.119 ± 30.827
1500 – 2700	Mid-elevation Hills	0.664 ± 0.350	0.021 ± 0.036	25.056 ± 3.042	0.696 ± 0.215	110.264 ± 61.070
2700 – 3900	Lower Mountain	0.769 ± 0.313	0.017 ± 0.019	25.184 ± 0.796	0.673 ± 0.164	132.520 ± 44.075
3900 – 5100	Mid-Mountain	0.927 ± 0.168	0.028 ± 0.022	25.166 ± 0.982	0.511 ± 0.307	162.639 ± 65.386
5100 – 6300	High Mountain	0.978 ± 0.083	0.143 ± 0.169	22.180 ± 1.391	0.037 ± 0.112	210.387 ± 18.654
6300 – 7424	High Himalayan Peaks	0.500 ± 0.000	0.500 ± 0.000	20.000 ± 0.000	0.500 ± 0.000	155.000 ± 0.000

extension to multi-gauge or spatially distributed calibration. In principle, additional gauge records can be incorporated into the pseudo-observed discharge field (Q_pseudo) by applying the same flow accumulation–based weighting approach, enabling simultaneous optimization against multiple spatial observations. Future work could explore multi-objective loss formulations that balance performance across gauges, further improving the spatial realism of parameter fields and streamflow predictions.

Conclusion

This study presents an end-to-end differentiable, gradient-based auto-calibration framework for a distributed glacio-hydrological model (PyGDM) in a Himalayan glacier-fed basin. By leveraging TensorFlow's automatic differentiation and an XLA-optimized routing scheme, the framework enables fully automated calibration of spatially and temporally varying parameters directly from discharge, substantially reducing human effort and computational cost compared to traditional trial-and-error approaches.

The proposed method consistently outperformed manual calibration, achieving higher predictive skill during calibration (NSE = 0.85; VD = -6.56) and validation (NSE =0.86; VD = −0.06), while maintaining physically interpretable parameter fields. Spatial and seasonal patterns of snowmelt, ice melt, surface runoff, and baseflow parameters captured realistic hydrological and cryospheric dynamics across land-use, elevation, and glacier classes. The smooth, monotonic convergence of the loss function demonstrated the robustness of gradient propagation through a fully differentiable, mass-conserving routing process, ensuring stable and physically consistent optimization. These results highlight that gradient-based, end-to-end differentiable calibration can simultaneously improve predictive accuracy and parameter interpretability, overcoming limitations of stochastic, heuristic, or lumped auto-calibration approaches.

Future work should explore multi-gauge calibration, multi-objective loss functions, GPU-accelerated training, and integration with climate or land-use change scenario**s** to extend applicability to larger basins and diverse hydroclimatic conditions. This framework provides a scalable, physically consistent, and computationally efficient approach for high-resolution hydrological modeling in data-limited mountainous regions, offering a robust tool for water resource assessment, hazard prediction, and climate impact studies in the Himalaya and comparable glacier-fed systems worldwide.

Code Availability

The source code for the differentiable PyGDM auto-calibration framework is publicly available at:
https://github.com/DineshJoshi2

Author Contributions

DJ developed the methodology, implemented the model framework, conducted the analysis, and wrote the manuscript. KLS and RBK provided supervision, contributed to validation of the results, and reviewed and edited the manuscript.

Data availability

Hydro-meteorological data are available from the DHM, Government of Nepal (2026,http://dhm.gov.np/).

References

Arendt, A., Bliss, A., Bolch, T., et al. (2017). Randolph Glacier Inventory – A dataset of global glacier outlines: Version 6.0. Technical report, Global Land Ice Measurements from Space, RGI Consortium. https://doi.org/10.7265/4m1f-gd79

Barco, J., Wong, K. M., & Stenstrom, M. K. (2008). Automatic calibration of the U.S. EPA SWMM model for a large urban catchment. Journal of Hydraulic Engineering, 134(4), 466–474. https://doi.org/10.1061/(ASCE)0733-9429(2008)134:4(466)

Bindas, T., Tsai, W. P., Liu, J., Rahmani, F., Feng, D., Bian, Y., et al. (2024). Improving river routing using a differentiable Muskingum–Cunge model and physics-informed machine learning. Water Resources Research, 60(1), e2023WR035337. https://doi.org/10.1029/2023WR035337

Buch, A., Mazumdar, H., & Pandey, P. (1993). Application of artificial neural networks in hydrological modeling: A case study of runoff simulation of a Himalayan glacier basin. Proceedings of the 1993 International Conference on Neural Networks (IJCNN-93-Nagoya, Japan), 25–29 October 1993, Nagoya, Japan. https://doi.org/10.1109/ijcnn.1993.714073

Cai, Q.-C., Hsu, T.-H., & Lin, J.-Y. (2021). Using the general regression neural network method to calibrate the parameters of a sub-catchment. Water, 13(8), 1089. https://doi.org/10.3390/w13081089

Chandel, V. S., & Ghosh, S. (2021). Components of Himalayan river flows in a changing climate. Water Resources Research, 57, e2020WR027589. https://doi.org/10.1029/2020WR027589

Chen, M., Qian, Z., Boers, N., Jakeman, A. J., Kettner, A. J., Brandt, M., et al. (2023). Iterative integration of deep learning in hybrid Earth surface system modelling. Nature Reviews Earth & Environment, 4(8), 568–581. https://doi.org/10.1038/s43017-023-00452-7

Feng, D., Liu, J., Lawson, K., & Shen, C. (2022). Differentiable, learnable, regionalized process-based models with multi-physical outputs can approach state-of-the-art hydrologic prediction accuracy. Water Resources Research, 58(10), e2022WR032404. https://doi.org/10.1029/2022WR032404

Feng, J., Duan, T., Bao, J., & Li, Y. (2024). An improved back propagation neural network framework and its application in the automatic calibration of storm water management model for an urban river watershed. Science of the Total Environment, 915, 169886. https://doi.org/10.1016/j.scitotenv.2024.169886

Feng, Y., Huang, X., & Ma, D. (2025). A comparative analysis of auto-calibration strategies for the urban hydrologic model. Hydrology Research, 56(8), 636–654. https://doi.org/10.2166/nh.2025.159

Gao, J., Liang, J., Lu, Y., Zhou, R., & Lu, X. (2023). Automatic SWMM parameter calibration method based on differential evolution and Bayesian optimization algorithm. Water, 15(20), 3582. https://doi.org/10.3390/w15203582

Garee, K., Chen, X., Bao, A., Wang, Y., & Meng, F. (2017). Hydrological modeling of the Upper Indus Basin: A case study from a high-altitude glacierized catchment Hunza. Water, 9(1), 17. https://doi.org/10.3390/w9010017

Höge, M., Scheidegger, A., Baity-Jesi, M., Albert, C., & Fenicia, F. (2022). Improving hydrologic models for predictions and process understanding using neural ODEs. Hydrology and Earth System Sciences, 26(19), 5085–5102. https://doi.org/10.5194/hess-26-5085-2022

Jafari, F., Jamshid Mousavi, S., Yazdi, J., & Kim, J. H. (2018). Real-time operation of pumping systems for urban flood mitigation: Single-period vs. multi-period optimization. Water Resources Management, 32(14), 4643–4660. https://doi.org/10.1007/s11269-018-2076-4

Jiang, S., Zheng, Y., & Solomatine, D. (2020). Improving AI system awareness of geoscience knowledge: Symbiotic integration of physical approaches and deep learning. Geophysical Research Letters, 47(13), e2020GL088229. https://doi.org/10.1029/2020GL088229

Joshi, D., Shrestha, K. L., Kayastha, R. B., & Kayastha, R. (2024). A hybrid approach to enhance streamflow simulation in data-constrained Himalayan basins: Combining the Glacio-hydrological Degree-Day Model and recurrent neural networks. Proceedings of the International Association of Hydrological Sciences, 387, 17–24. https://doi.org/10.5194/piahs-387-17-2024

Kang, T., & Lee, S. (2014). Modification of the SCE-UA to include constraints by embedding an adaptive penalty function and application approach. Water Resources Management, 28(8), 2145–2159. https://doi.org/10.1007/s11269-014-0602-6

Karra, K., Kontgis, C., Statman-Weil, Z., Mazzariello, J. C., Mathis, M., & Brumby, S. P. (2021). Global land use/land cover with Sentinel-2 and deep learning. In 2021 IEEE International Geoscience and Remote Sensing Symposium (IGARSS) (pp. 11–16). IEEE. https://doi.org/10.1109/igarss47720.2021.9553499

Kayastha, R. B., Steiner, N., Kayastha, R., Mishra, S. K., & McDonald, K. (2020). Comparative study of hydrology and icemelt in three Nepal river basins using the Glacio-Hydrological Degree-Day Model (GDM) and observations from the Advanced Scatterometer (ASCAT). Frontiers in Earth Science, 7, 354. https://doi.org/10.3389/feart.2019.00354

Khu, S. T., & Werner, M. G. F. (2003). Reduction of Monte-Carlo simulation runs for uncertainty estimation in hydrological modelling. Hydrology and Earth System Sciences, 7(5), 680–692. https://doi.org/10.5194/hess-7-680-2003

Kraft, B., Jung, M., Körner, M., Koirala, S., & Reichstein, M. (2022). Towards hybrid modeling of the global hydrological cycle. Hydrology and Earth System Sciences, 26(6), 1579–1614. https://doi.org/10.5194/hess-26-1579-2022

Lee, D.-H., & Kang, D.-S. (2016). The application of the artificial neural network ensemble model for simulating streamflow. Procedia Engineering, 154, 1217–1224. https://doi.org/10.1016/j.proeng.2016.07.434

Leta, O. T., Van Griensven, A., & Bauwens, W. (2017). Effect of single and multisite calibration techniques on the parameter estimation, performance, and output of a SWAT model of a spatially heterogeneous catchment. Journal of Hydrologic Engineering, 22(3), 05016036. https://doi.org/10.1061/(ASCE)HE.1943-5584.0001471

Li, L., Shen, M., Hou, Y., Xu, C.-Y., Lutz, A. F., Chen, J., et al. (2019). Twenty-first-century glacio-hydrological changes in the Himalayan headwater Beas River basin. Hydrology and Earth System Sciences, 23, 1483–1503. https://doi.org/10.5194/hess-23-1483-2019

Li, Y., Ma, L., Huang, J., Disse, M., Zhan, W., Li, L., Zhang, T., Sun, H., & Tian, Y. (2024). Machine learning parallel system for integrated process-model calibration and accuracy enhancement in sewer-river systems. Environmental Science and Ecotechnology, 18, 100320. https://doi.org/10.1016/j.ese.2023.100320

Luo, Y., Arnold, J., Allen, P., & Chen, X. (2012). Baseflow simulation using SWAT model in an inland river basin in Tianshan Mountains, Northwest China. Hydrology and Earth System Sciences, 16, 1259–1267. https://doi.org/10.5194/hess-16-1259-2012

Ma, B., Wu, Z., Hu, C., Wang, H., Xu, H., & Yan, D. (2022). Process-oriented SWMM real-time correction and urban flood dynamic simulation. Journal of Hydrology, 605, 127269. https://doi.org/10.1016/j.jhydrol.2022.127269

Pang, B., Shi, S., Zhao, G., Shi, R., Peng, D., & Zhu, Z. (2020). Uncertainty assessment of urban hydrological modelling from a multiple objective perspective. Water, 12(5), 1393. https://doi.org/10.3390/w12051393

Reichstein, M., Camps-Valls, G., Stevens, B., Jung, M., Denzler, J., Carvalhais, N., & Prabhat, F. (2019). Deep learning and process understanding for data-driven Earth system science. Nature, 566(7743), 195–204. https://doi.org/10.1038/s41586-019-0912-1

Schmid, F., & Leandro, J. (2023). An ensemble data-driven approach for incorporating uncertainty in the forecasting of stormwater sewer surcharge. Urban Water Journal, 20(9), 1140–1156. https://doi.org/10.1080/1573062X.2023.2240309

Schneider, K. E., & Hogue, T. S. (2022). Calibration of a hydrologic model in data-scarce Alaska using satellite and other gridded products. Journal of Hydrology: Regional Studies, 39, 100979. https://doi.org/10.1016/j.ejrh.2021.100979

Shahed Behrouz, M., Zhu, Z., Matott, L. S., & Rabideau, A. J. (2020). A new tool for automatic calibration of the Storm Water Management Model (SWMM). Journal of Hydrology, 581, 124436. https://doi.org/10.1016/j.jhydrol.2019.124436

Sheikholeslami, R., & Razavi, S. (2017). Progressive Latin hypercube sampling: An efficient approach for robust sampling-based analysis of environmental models. Environmental Modelling & Software, 93, 109–126. https://doi.org/10.1016/j.envsoft.2017.03.010

Shrestha, K. L., Kayastha, R. B., & Kayastha, R. (2024). Coupling the Glacio-hydrological Degree-day Model (GDM) with PCRaster for spatial dynamic modeling of Himalayan river basins. Proceedings of the International

Association of Hydrological Sciences, 387, 25–31. https://doi.org/10.5194/piahs-387-25-2024

Shrestha, M., Koike, T., Hirabayashi, Y., Xue, Y., Wang, L., Rasul, G., & Ahmad, B. (2015). Integrated simulation of snow and glacier melt in a water and energy balance-based, distributed hydrological modeling framework at Hunza River basin of Pakistan Karakoram region. Journal of Geophysical Research, 120, 4889–4919. https://doi.org/10.1002/2014JD022666

Shukla, S., Jain, S. K., & Kansal, M. L. (2021). Hydrological modelling of a snow/glacier-fed western Himalayan basin to simulate the current and future streamflows under changing climate scenarios. Science of the Total Environment, 795, 148871. https://doi.org/10.1016/j.scitotenv.2021.148871

Sun, A. Y., Jiang, P., Yang, Z.-L., Xie, Y., & Chen, X. (2022). A graph neural network (GNN) approach to basin-scale river network learning: The role of physics-based connectivity and data fusion. Hydrology and Earth System Sciences, 26(19), 5163–5184. https://doi.org/10.5194/hess-26-5163-2022

Sun, R., Duan, Q., & Huo, X. (2021). Multi-objective adaptive surrogate modeling-based optimization for distributed environmental models based on grid sampling. Water Resources Research, 57(11), e2020WR028740. https://doi.org/10.1029/2020WR028740

Sun, R., Hernández, F., Liang, X., & Yuan, H. (2020). A calibration framework for high-resolution hydrological models using a multiresolution and heterogeneous strategy. Water Resources Research, 56(8), e2019WR026541. https://doi.org/10.1029/2019WR026541

Tiwari, M. K., & Chatterjee, C. (2010). Uncertainty assessment and ensemble flood forecasting using bootstrap-based artificial neural networks (BANNs). Journal of Hydrology, 382(1), 20–33. https://doi.org/10.1016/j.jhydrol.2009.12.013

Tongal, H., & Booij, M. J. (2017). Quantification of parametric uncertainty of ANN models with GLUE method for different streamflow dynamics. Stochastic Environmental Research and Risk Assessment, 31(4), 993–1010. https://doi.org/10.1007/s00477-017-1408-x

Wang, C., Jiang, S., Zheng, Y., Han, F., Kumar, R., Rakovec, O., & Li, S. (2024). Distributed hydrological modeling with physics-encoded deep learning: A general framework and its application in the Amazon. Water Resources Research, 60(4). https://doi.org/10.1029/2023WR036170

Wang, H., Lei, X., Khu, S.-T., & Song, L. (2019). Optimization of pump start-up depth in drainage pumping station based on SWMM and PSO. Water, 11(5), 1002. https://doi.org/10.3390/w11051002

Wang, N., Liu, W., Wang, H., Sun, F., Duan, W., Li, Z., Li, Z., & Chen, Y. (2021). Improving streamflow and flood simulations in three headwater catchments of the Tarim River based on a coupled glacier-hydrological model. Journal of Hydrology, 603, 127048. https://doi.org/10.1016/j.jhydrol.2021.127048

Wu, Z., Ma, B., Wang, H., Hu, C., Lv, H., & Zhang, X. (2021). Identification of sensitive parameters of urban flood model based on artificial neural network. Water Resources Management, 35(7), 2115–2128. https://doi.org/10.1007/s11269-021-02825-3

Wulf, H., Bookhagen, B., & Scherler, D. (2016). Differentiating between rain, snow, and glacier contributions to river discharge in the western Himalaya using remote-sensing data and distributed hydrological modeling. Advances in Water Resources, 88, 152–169. https://doi.org/10.1016/j.advwatres.2015.12.004

Xu, T., Longyang, Q., Tyson, C., Zeng, R., & Neilson, B. T. (2022). Hybrid physically based and deep learning modeling of a snow-dominated, mountainous, Karst watershed. Water Resources Research, 58(3), e2021WR030993. https://doi.org/10.1029/2021WR030993

Xue, F., Tian, J., Wang, W., Zhang, Y., & Ali, G. (2020). Parameter calibration of SWMM model based on optimization algorithm. Computers, Materials & Continua, 65(3), 2189–2199. https://doi.org/10.32604/cmc.2020.06513

Zhang, Z., Hu, W., Wang, W., Zhou, J., Liu, D., Qi, X., & Zhao, X. (2022). The hydrological effect and uncertainty assessment by runoff indicators based on SWMM for various LID facilities. Journal of Hydrology, 613, 128418. https://doi.org/10.1016/j.jhydrol.2022.128418

Zhao, D., Chen, J., Wang, H., & Tong, Q. (2013). Application of a sampling based on the combined objectives of parameter identification and uncertainty analysis of an urban rainfall-runoff model. Journal of Irrigation and Drainage Engineering, 139(1), 66–74. https://doi.org/10.1061/(ASCE)ir.1943-4774.0000522

Zhong, B., Wang, Z., Yang, H., Xu, H., Gao, M., & Liang, Q. (2022). Parameter optimization of SWMM

model using integrated Morris and GLUE methods. Water, 15(1), 149. https://doi.org/10.3390/w15010149